

Local structure evolution in polycrystalline $\text{Zn}_{1-x}\text{Mg}_x\text{O}$ ($0 \leq x \leq 0.15$) studied by Raman and by synchrotron x-ray pair distribution analysis

Young-Il Kim, Katharine Page, Andi M. Limarga, David R. Clarke, and Ram Seshadri
*Materials Department and Materials Research Laboratory,
University of California, Santa Barbara, CA 93106*

(Dated: August 10, 2021)

The local structures of $\text{Zn}_{1-x}\text{Mg}_x\text{O}$ alloys have been studied by Raman spectroscopy and by synchrotron x-ray pair distribution function (PDF) analysis. Within the solid solution range ($0 \leq x \leq 0.15$) of $\text{Zn}_{1-x}\text{Mg}_x\text{O}$, the wurtzite framework is maintained with Mg homogeneously distributed throughout the wurtzite lattice. The E_2^{high} Raman line of $\text{Zn}_{1-x}\text{Mg}_x\text{O}$ displays systematic changes in response to the evolution of the crystal lattice upon the Mg-substitution. The red-shift and broadening of the E_2^{high} mode are explained by the expansion of hexagonal ab -dimensions, and compositional disorder of Zn/Mg, respectively. Synchrotron x-ray PDF analyses of $\text{Zn}_{1-x}\text{Mg}_x\text{O}$ reveal that the Mg atoms have a slightly reduced wurtzite parameter u and more regular tetrahedral bond distances than the Zn atoms. For both Zn and Mg, the internal tetrahedral geometries are independent of the alloy composition.

PACS numbers: 61.10.Nz, 71.55.Gs, 77.22.Ej

I. INTRODUCTION

Polar semiconductors such as wurtzite ZnO and GaN have great potential for use in the polarization-doped field effect transistors (PolFETs) which exploit a polarization gradient at the channel layer to attain higher mobility and higher concentrations of carriers. The performance of PolFETs depends primarily on the interface quality and the magnitude of the polarization gradient at the heterojunction. Those goals can be approached by interfacing a polar semiconductor with its alloy derivative, as exemplified by the fabrication of a PolFET comprising the interface of GaN/ $\text{Ga}_{1-x}\text{Al}_x\text{N}$ ($x = 0 - 0.3$).¹ In designing ZnO-based PolFETs, $\text{Zn}_{1-x}\text{Mg}_x\text{O}$ alloys can be considered as the sub-layer component, since Mg-substitution effectively alters the polarization of ZnO while keeping the lattice dimensions nearly unchanged.²

In a previous report,² we have outlined the prospects for ZnO/ $\text{Zn}_{1-x}\text{Mg}_x\text{O}$ heterojunctions for PolFET applications, based on structural analysis of $\text{Zn}_{1-x}\text{Mg}_x\text{O}$ alloys using synchrotron x-ray diffraction. We showed that the ionic polarization can be tuned by $\approx 14\%$ from ZnO to $\text{Zn}_{0.85}\text{Mg}_{0.15}\text{O}$, despite only small changes in the cell volume ($\approx 0.3\%$). Also, it was found that Mg can substitute up to 15% of total Zn in the wurtzite lattice, without any evidence for segregation. While the average crystal structures of $\text{Zn}_{1-x}\text{Mg}_x\text{O}$ phases were accurately determined in the above study, there still remain the local structural details of the solid solutions to be understood. Therefore in a continuing effort, we have performed Raman studies and synchrotron x-ray pair distribution function (PDF) analysis of polycrystalline $\text{Zn}_{1-x}\text{Mg}_x\text{O}$ samples. Raman spectroscopy is known to be useful for examining compositional disorder and/or the presence of strain within semiconductor alloys.^{3,4,5,6,7,8} In previous Raman studies on wurtzite type crystals, the peak position and shape of the E_2^{high} phonon mode have been used to investigate the effects of sample grain size, heterogeneous components,

and defects.^{5,6} PDF analysis provides a powerful probe of local non-periodic atomic displacements in the short range, and is a suitable complement to the k -space refinement technique.^{9,10} This ability is very relevant to the possible distinction of tetrahedral out-of center displacements of Zn and Mg, and provides for a better comparison platform with density functional calculations of the crystal structure.

In this study, we provide a complete description of polycrystalline $\text{Zn}_{1-x}\text{Mg}_x\text{O}$ alloys prepared from crystalline $\text{Zn}_{1-x}\text{Mg}_x(\text{C}_2\text{O}_4) \cdot 2\text{H}_2\text{O}$ precursors. We present results of thermogravimetry, ultraviolet/visible diffuse-reflectance spectroscopy, infrared, and Raman spectroscopy in addition to examining the distinct tetrahedral geometries of Zn and Mg using synchrotron x-ray PDF analyses based on supercell structure models.

II. EXPERIMENTAL

Powder samples of $\text{Zn}_{1-x}\text{Mg}_x\text{O}$ ($x = 0, 0.05, 0.10,$ and 0.15) were prepared using an oxalate precursor route as described previously.² Aqueous solutions of zinc acetate, magnesium acetate, and oxalic acid were separately prepared and mixed to precipitate zinc magnesium oxalates, which are crystalline, single-phase compounds with Zn^{2+} and Mg^{2+} homogeneously mixed at the atomic level. The precipitates were thoroughly washed with deionized water and dried at 60°C for 4h to produce white powders of $\text{Zn}_{1-x}\text{Mg}_x(\text{C}_2\text{O}_4) \cdot 2\text{H}_2\text{O}$, as verified by powder x-ray diffraction. Subsequently the oxalate dihydrates were transformed to $\text{Zn}_{1-x}\text{Mg}_x\text{O}$ by heating in air at 550°C for 24h. The thermal decomposition of $\text{Zn}_{1-x}\text{Mg}_x(\text{C}_2\text{O}_4) \cdot 2\text{H}_2\text{O}$ was monitored by thermogravimetry using a Cahn ThermMax 400 thermogravimetric analyzer (Thermo Scientific). For each composition, ≈ 60 mg of powder was heated in air up to 1000°C at 5°C min^{-1} . Fourier-transform infrared (FT-IR) spec-

tra of $\text{Zn}_{1-x}\text{Mg}_x\text{O}$ powders were recorded in KBr using a Nicolet Magna 850 FT-IR spectrophotometer in the transmission mode. Diffuse-reflectance absorption spectra were measured for $\text{Zn}_{1-x}\text{Mg}_x\text{O}$ in the wavelength range of 220–800 nm using a Shimadzu UV-3600 spectrophotometer equipped with an ISR-3100 integrating sphere. The powder samples were mounted to have flat surfaces and ≈ 1.5 mm thickness. The optical band gap was determined by extrapolating the linear part of absorption edge to zero-absorption level. Raman measurements were conducted at room temperature using an optical microprobe fitted with a single monochromator (Jobin-Yvon, T64000). Powder samples were compacted on frosted glass plates and spectra were recorded in backscattering geometry using a 488.08 nm Ar^+ laser with a beam power of 50 mW and a spot size of ≈ 2 μm . For each sample, five acquisitions of 30 s exposure were performed and the averaged spectra are reported. The E_2^{high} phonon mode was chosen for detailed peak profile analyses. The spectral background was removed following Shirley,¹¹ and Breit-Wigner type peak fitting¹² was employed to determine peak position and the width.

Synchrotron x-ray scattering experiments were carried out at beam line 11-ID-B of the Advanced Photon Source (Argonne National Laboratory) using an x-ray energy of 90.8 keV ($\lambda \approx 0.1365$ \AA) at room temperature. Use of high energy radiation enables data acquisition at high Q ($=4\pi\sin\theta/\lambda$) wave vector, which in turn improves the reliability of the Fourier transformation for obtaining the PDF $G(r)$. In the present work, scattering data with Q_{max} of 28 \AA^{-1} were utilized for extracting PDFs. Sample powders were loaded in Kapton tubes and data were measured in the transmission mode using an amorphous silicon image plate system (General Electric Healthcare). For each sample, 33 images were taken with an exposure time of 16 s per image. The program FIT2D¹³ was used to convert images into the corresponding one-dimensional x-ray diffraction (XRD) pattern. The average crystal structures of these samples have been determined by Rietveld method and reported previously.² For obtaining the PDF from XRD data, the program PDFGETX2 was used.¹⁴ First the measured scattering intensities were corrected for sample container background, Compton scattering, and Laue diffuse scattering. Next the coherently scattered intensities $I(Q)$ were normalized in absolute electron units to give total scattering structure functions $S(Q)$. Finally the reduced structure functions $F(Q) = Q[S(Q) - 1]$ were Fourier-transformed to produce the atomic PDFs $G(r)$. The refinements of $\text{Zn}_{1-x}\text{Mg}_x\text{O}$ structures were performed against the above obtained experimental PDFs using the software PDFFIT.¹⁵

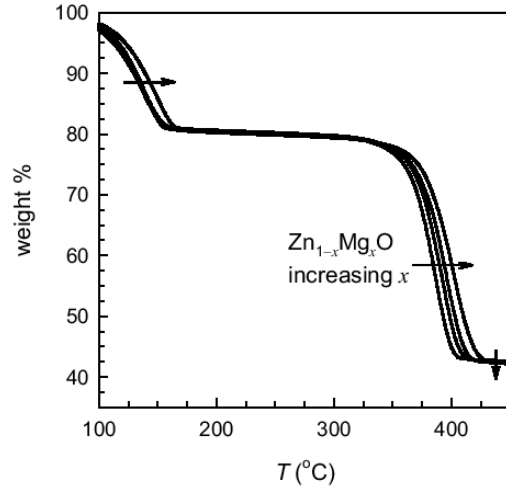


FIG. 1: Thermogravimetry of $\text{Zn}_{1-x}\text{Mg}_x\text{O}$ ($x = 0, 0.05, 0.10,$ and 0.15) in air at a heating rate 5°C min^{-1} .

III. RESULTS

A. Sample characterization

The thermogravimetric profiles of $\text{Zn}_{1-x}\text{Mg}_x(\text{C}_2\text{O}_4)\cdot 2\text{H}_2\text{O}$ ($x = 0, 0.05, 0.10,$ and 0.15) are shown in Fig. 1. The stepwise processes of dehydration and oxalate-to-oxide conversion are clearly observed at around 130 and 390°C, respectively,¹⁶ with the weight changes in good agreements with calculated estimates. With increase of Mg content, the onset temperatures of both weight loss steps shifted to higher temperatures. This could be interpreted as indicative of the extra activation barrier for stabilizing Mg in the wurtzite lattice. For all cases, oxide formation was nearly complete at 500°C without any noticeable weight change at higher temperature. It is therefore assumed that isothermal heating at 550°C for 24 h completely transforms $\text{Zn}_{1-x}\text{Mg}_x(\text{C}_2\text{O}_4)\cdot 2\text{H}_2\text{O}$ to the oxides $\text{Zn}_{1-x}\text{Mg}_x\text{O}$.

In Fig. 2, the FT-IR spectra for $\text{Zn}_{1-x}\text{Mg}_x\text{O}$ are shown, which are consistent with the registered reference data of wurtzite ZnO.¹⁷ A previous report suggested that organic precursors for ZnO synthesis may leave carbonate species strongly bound within the lattice,¹⁸ but the samples in this study did not exhibit any spectral feature at ≈ 1300 and ≈ 1500 cm^{-1} demonstrating the complete combustion of oxalate.¹⁹ The wurtzite lattice vibrations were observed as broad IR bands at 400–600 cm^{-1} . Upon Mg-substitution, these stretching modes shifted to higher wavenumber as a result of the smaller reduced mass of Mg–O compared with that of Zn–O.

The optical band gaps (E_g) of $\text{Zn}_{1-x}\text{Mg}_x\text{O}$ powders were determined from the diffuse-reflectance absorption spectra as shown in Fig. 3. The absorbance (A) of the samples were obtained from the measured reflectance (R)

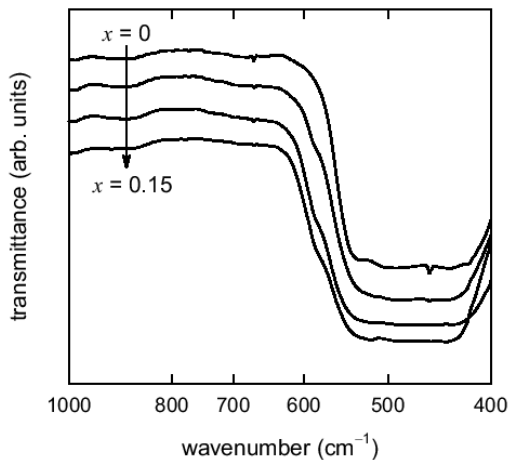


FIG. 2: FT-IR spectra of $\text{Zn}_{1-x}\text{Mg}_x\text{O}$ ($x = 0, 0.05, 0.10,$ and 0.15).

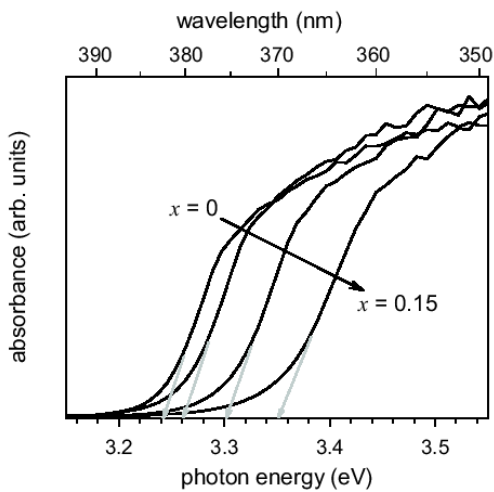


FIG. 3: Diffuse-reflectance absorption spectra for $\text{Zn}_{1-x}\text{Mg}_x\text{O}$ ($x = 0, 0.05, 0.10,$ and 0.15). For each spectrum, the band gap energy is indicated by the extrapolated arrow.

according to the Kubelka-Munk relation.²⁰

$$A = \frac{(1 - R)^2}{2R} \quad (1)$$

In the present measurement setup, the sample analytes are thick enough (≈ 1.5 mm) to disallow transmission, and the Kubelka-Munk theory is appropriate. As clearly seen in Fig. 3, the absorption edges are shifted to the higher energy side with the increase of Mg content x . Also noticed are slight broadenings of the edge slopes upon the Mg-substitution. The band gap energy gradually increased from 3.24 ($x = 0$) to 3.26 ($x = 0.05$), 3.30 ($x = 0.10$), and 3.35 eV ($x = 0.15$). In previous studies on $\text{Zn}_{1-x}\text{Mg}_x\text{O}$ thin films grown by pulsed laser deposition, Ohtomo *et al.* have observed a similar composition-dependence of the band gaps; monotonic increases from

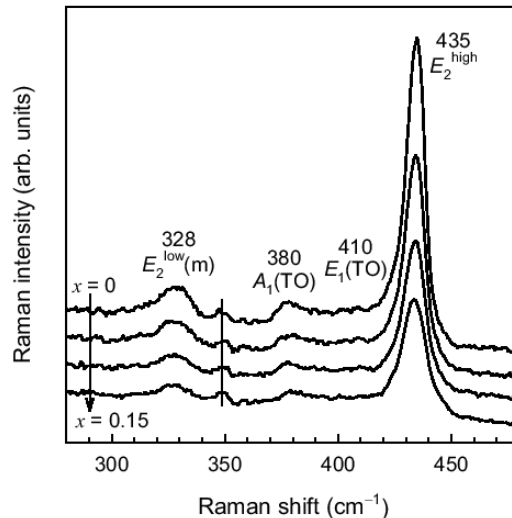


FIG. 4: Raman spectra of the $\text{Zn}_{1-x}\text{Mg}_x\text{O}$ ($x = 0, 0.05, 0.10,$ and 0.15). A plasma line from the 488.08 nm Ar^+ laser appears at $\approx 348 \text{ cm}^{-1}$ (indicated by a vertical line).

3.30 ($x = 0$) to 3.63 eV ($x = 0.14$).²¹ Their absolute band gap energies are not exactly reproduced in our polycrystalline samples, but this may be due to the differences in experimental details. The optical band gaps of solids are frequently determined to be different depending on sample type, optical characterization technique, and band gap determination method.^{22,23} In the above study on $\text{Zn}_{1-x}\text{Mg}_x\text{O}$ films the band gaps were evaluated with the assumption $\alpha^2 \propto (h\nu - E_g)$, in which the absorption coefficient α was deduced from the transmittance measurements.

B. Raman spectroscopy

Wurtzite ZnO belongs to the space group C_{6v}^4 (Hermann-Mauguin symbol $P6_3mc$) and has six lattice phonon modes, $A_1 + 2B_1 + E_1 + 2E_2$, of which the B_1 branches are Raman inactive.^{24,25} The A_1 and E_1 modes are polarized along the z -direction and xy -plane, respectively, whereas the two E_2 modes (E_2^{low} and E_2^{high}) are non-polar.^{24,25,26} Each of the polar modes is split to longitudinal (LO) and transverse optical (TO) components due to the macroscopic electric field associated with the LO phonons.

Raman spectra of polycrystalline $\text{Zn}_{1-x}\text{Mg}_x\text{O}$ powders were examined over the frequency range 90–830 cm^{-1} and part of those spectra are presented in Fig. 4. For all cases of $x = 0 - 0.15$, the measured Raman spectra agree well with the wurtzite ZnO vibration modes, without any new bands arising from Mg-substitution. Raman features characteristic of cubic MgO ²⁷ were not observed. In previous Raman studies on ZnO films or nanophases doped with N, Al, Ga, Sb, Fe, Mn, or Mg, additional bands have been observed and attributed to the induced lattice de-

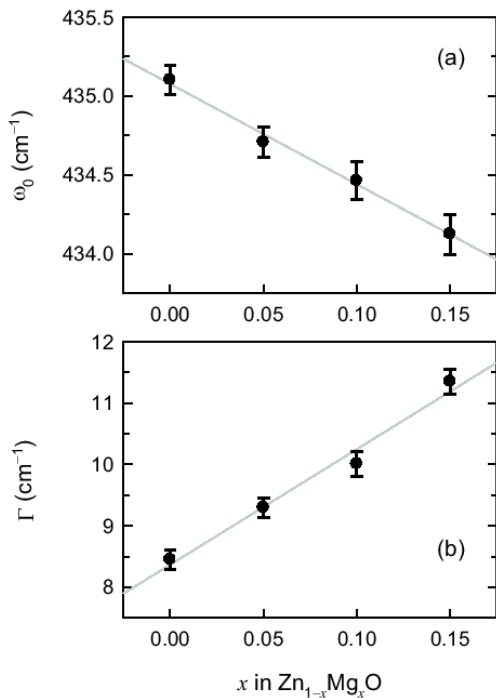


FIG. 5: (a) phonon frequency ω_0 and (b) width Γ of Raman E_2^{high} mode as functions of Mg content in $\text{Zn}_{1-x}\text{Mg}_x\text{O}$. Gray lines are best linear fits.

fect or the dopants' local vibration.^{28,29,30} A previous Raman study of polycrystalline $\text{Zn}_{1-x}\text{Mg}_x\text{O}$ has shown that the Mg-substitution flattens the overall Raman signal.³¹ In Fig. 4, the Raman peaks from $A_1(\text{TO})$, $E_1(\text{TO})$, E_2^{low} (multiphonon), and E_2^{high} modes are found. The A_1 and E_1 modes reflect the strength of the polar lattice bonds, which are of interest in relation with the c -axial displacements of cations. However the peaks corresponding to those two modes were not well resolved from the background and could not be used for a detailed study. Usually Raman signals from polar modes are weaker in intensity due to phonon-plasmon interactions.³² The E_2^{high} phonon, which is the most prominent in the ZnO Raman spectra, was used for the peak profile analysis. The Raman line shape was fitted using the Breit-Wigner function,

$$I(\omega) \propto \frac{1 + 2\beta(\omega - \omega_0)/\Gamma^2}{1 + [2(\omega - \omega_0)/\Gamma]^2} \quad (2)$$

where $I(\omega)$ is the Raman intensity at a given frequency, ω_0 is the Raman shift, Γ is the broadening expressed as full-width at half-maximum (FWHM), and β is an asymmetry parameter ($\beta = 0$ for the symmetrical peak).¹² For each Raman spectrum of $\text{Zn}_{1-x}\text{Mg}_x\text{O}$, the E_2^{high} phonon frequency ω_0 was determined along with Γ , as plotted in Fig. 5.

If we consider the mass change in the Mg-substitution for Zn, the phonon frequency is expected to increase for

the samples with higher x . But the observed trend is contrary to this: The E_2^{high} phonon frequency decreases upon the Mg-substitution. To explain this, it should be recalled that the E_2^{high} mode of ZnO corresponds mostly ($\approx 85\%$) to the vibration of oxygen atoms,³³ and is insensitive to the mass substitution on the cation site. On the other hand, since the E_2^{high} mode is associated with atomic motions on the xy -plane, its phonon energy depends on the in-plane lattice dimensions. In the $\text{Zn}_{1-x}\text{Mg}_x\text{O}$ solid solution, the hexagonal parameter a monotonically increases with x , hence softening the E_2^{high} phonon mode. The decrease of E_2^{high} mode frequency has been similarly observed from ZnO thin films under the tensile strain along the xy -plane.³⁴

In addition to the frequency shift, it is also noted that the E_2^{high} peaks are markedly broadened upon the Mg-substitution. The Raman mode frequency and the peak width can be influenced by the random substitution of Zn with Mg through the compositional disorder effect.^{5,6,35} As inferred from the evolution of average crystal structures in $\text{Zn}_{1-x}\text{Mg}_x\text{O}$, the Mg atoms do not have an identical bonding geometry to that of Zn. In other words the Mg-substitution alters the translational symmetry of the wurtzite lattice to modify the phonon oscillation field. In previous Raman studies on the alloy systems, the spatial correlation has been regarded an adequate mechanism responsible for the red-shift of the mode frequency as well as the peak broadening.^{5,6,35} The model is based on the wave vector uncertainty, $\Delta q = 2\pi/L$, where q is the phonon wave vector range, L is the length scale of phonon confinement, and q has the phonon dispersion relation $\omega(q)$ with the Raman frequency. It predicts that, as the L becomes smaller, Δq becomes larger so that a wider range of frequencies is allowed for Raman scattering.

In $\text{Zn}_{1-x}\text{Mg}_x\text{O}$ compounds as well, the presence of the hetero component Mg seems to perturb the wurtzite phonon modes. As shown in Fig. 5, both the frequency shift and the peak broadening become greater for the samples with higher Mg-concentration. However, the symmetry of E_2^{high} peak shape did not show significant dependences on the Mg-concentration, which is somewhat unexpected. This is in contrast to the spatial correlation model and also with the experimental examples of disordered semiconductor crystals, where the Raman line shapes become more asymmetric as the peak widths increase.^{5,6}

C. Pair distribution functions

Both Rietveld refinement and PDF analysis utilize one-dimensional diffraction patterns to extract crystal structure information. The former focuses on the long range average structure based on Bragg diffraction, while the latter focuses on the local structure information over short length scales from the diffuse scattering in addition to the Bragg diffraction.^{9,10,36,37,38} Therefore the above

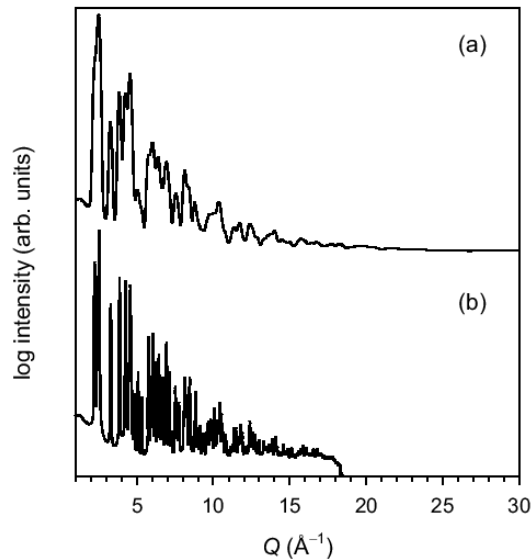


FIG. 6: XRD patterns of $\text{Zn}_{0.95}\text{Mg}_{0.05}\text{O}$, used for (a) PDF analysis and (b) Rietveld refinement. Sample-to-detector distances were 150 mm for (a) and 660 mm for (b).

two methods rely on distinct data qualities. The diffuse scattering becomes more prominent at high Q , for which the PDF data require very large Ewald spheres, but not necessarily very high resolution, and extremely large signal to noise ratios. For Rietveld analyses, highly resolved Bragg peaks are preferred, at the expense of collecting data over smaller Ewald spheres. In order to meet both needs, the diffraction experiments were carried out at two different sample-to-detector distances, 150 mm for the PDF data and 660 mm for the Rietveld data. Fig. 6 compares the two XRD patterns of $\text{Zn}_{0.95}\text{Mg}_{0.05}\text{O}$, one used for Rietveld refinement and the other for PDF study. The pattern for Rietveld refinement comprised sharp and well-resolved Bragg peaks but the diffraction information rapidly vanishes at Q beyond 18 \AA^{-1} . However, in the pattern for PDF analysis the scattering intensities are observable at Q as high as 30 \AA^{-1} .

The PDF data $G(r)$ for the four samples of $\text{Zn}_{1-x}\text{Mg}_x\text{O}$ ($x = 0, 0.05, 0.10, \text{ and } 0.15$) were obtained following a standard data processing sequence.^{14,39} In Fig. 7, the PDFs from different $\text{Zn}_{1-x}\text{Mg}_x\text{O}$ compositions are superimposed, and it is observed that the data are hardly distinguished. Since the average crystal structures (lattice symmetry, lattice parameters, atomic positions, *etc.*) of $\text{Zn}_{1-x}\text{Mg}_x\text{O}$ phases are similar, the composition-dependent changes in PDFs are not immediately noticeable. However a close view at the PDF peak at $r \approx 2 \text{ \AA}$ exposes a subtle evolution in the coordination shell of the nearest cation–anion bond pairs. As the Mg content increases, these PDF peaks are slightly shifted to longer r , with gradual increases of peak heights. This finding is consistent with the previous Rietveld refinement result which indicated that the (Zn,Mg)–O bond distances become more regular upon Mg-substitution.² The first shell

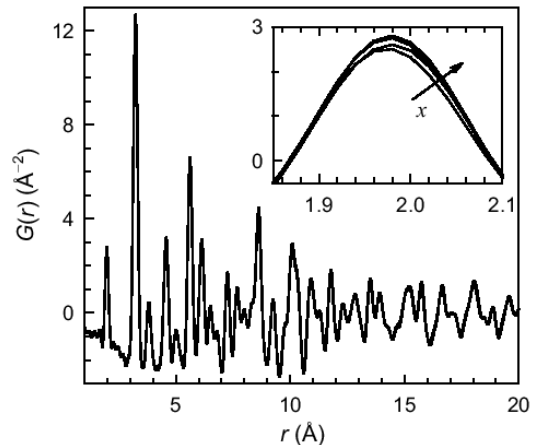


FIG. 7: Experimental PDFs for $\text{Zn}_{1-x}\text{Mg}_x\text{O}$ phases with $x = 0, 0.05, 0.10, \text{ and } 0.15$. Inset shows the zoomed-in view of the peak corresponding to the first coordination (Zn,Mg)–O shell.

interatomic distances are $(3 \times)1.9731 \text{ \AA}$ and 1.9941 \AA in ZnO , and $(3 \times)1.9756 \text{ \AA}$ and 1.9873 \AA in $\text{Zn}_{0.85}\text{Mg}_{0.15}\text{O}$. Although small in magnitudes, the above changes correspond to $\approx 45\%$ reduction in the standard deviation of the four bond distances, which result in the discernible peak sharpening. The shifts of peak positions can be ascribed to the lengthening of the three shorter bonds rather than a change in the longer apical bond.

The real space PDF data are therefore useful for directly depicting the bonding geometry in a specific r -range. For more detailed and quantitative information, the PDF data were analyzed by full profile refinements using several different models of simple cell as well as supercell. The simple cell models were based on the hexagonal wurtzite structure (space group $P6_3mc$, $Z = 2$, $a \approx 3.25 \text{ \AA}$, $c \approx 5.20 \text{ \AA}$) with O at $(\frac{1}{3} \frac{2}{3} 0)$ and Zn/Mg at $(\frac{1}{3} \frac{2}{3} u)$. In the analyses using the simple cell, the fractional occupancies of Zn and Mg were set according to the composition of each phase $\text{Zn}_{1-x}\text{Mg}_x\text{O}$ ($x = 0, 0.05, 0.10, \text{ and } 0.15$). Supercell model structures were constructed by expanding the wurtzite simple cell to a $3 \times 3 \times 1$ size ($Z = 18$, $a \approx 9.75 \text{ \AA}$, $c \approx 5.20 \text{ \AA}$). By partially replacing the Zn atoms with Mg, the parent $\text{Zn}_{18}\text{O}_{18}$ supercell can be modified to the compositions $\text{Zn}_{17}\text{MgO}_{18}$ ($\text{Zn}_{0.944}\text{Mg}_{0.056}\text{O}$), $\text{Zn}_{16}\text{Mg}_2\text{O}_{18}$ ($\text{Zn}_{0.889}\text{Mg}_{0.111}\text{O}$), and $\text{Zn}_{15}\text{Mg}_3\text{O}_{18}$ ($\text{Zn}_{0.833}\text{Mg}_{0.167}\text{O}$) to model the $x = 0.05, 0.10, \text{ and } 0.15$ phases, respectively. The Mg atoms in $\text{Zn}_{16}\text{Mg}_2\text{O}_{18}$ and $\text{Zn}_{15}\text{Mg}_3\text{O}_{18}$ models were separated to be as distant from one another as allowed by the cell. PDF refinements^{15,38} of $G(r)$ were carried out using the variables of scale factor, dynamic correlation factor, resolution factor, lattice constants, independent u of Zn and Mg, and isotropic temperature factors of Zn, Mg, and O.

First the PDF refinements were performed for $\text{Zn}_{1-x}\text{Mg}_x\text{O}$ ($x = 0, 0.05, 0.10, \text{ and } 0.15$) using the four-atom simple cell models, in which the cation composi-

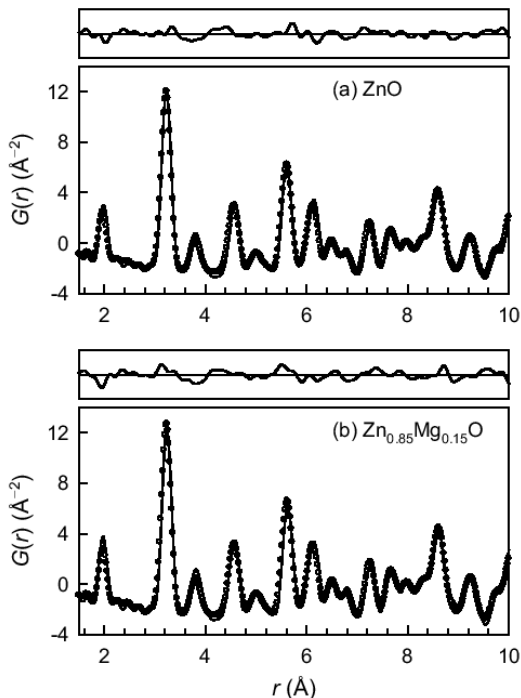


FIG. 8: PDF refinement profiles for (a) ZnO and (b) $\text{Zn}_{0.85}\text{Mg}_{0.15}\text{O}$, using four-atom simple cell models. Experimental (open circles) and calculated (solid lines) data are plotted in the bottom panels, along with the difference patterns ($G_{\text{expt}} - G_{\text{calc}}$) in the top panels.

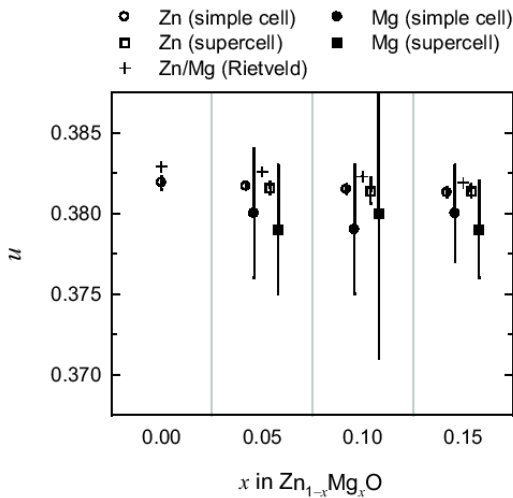


FIG. 9: Position parameters for Mg and Zn in $\text{Zn}_{1-x}\text{Mg}_x\text{O}$ phases, as analyzed by PDF refinements (1.5–10 Å) of simple cell and $3 \times 3 \times 1$ supercell model structures. Rietveld refinement results² are also compared. For the PDF results, error bars indicate one estimated-standard-deviation (esd) while for the Rietveld results, the symbol height corresponds to one esd.

TABLE I: Summary of PDF refinements for $\text{Zn}_{1-x}\text{Mg}_x\text{O}$ ($x = 0, 0.05, 0.10,$ and 0.15) using simple cell models, over the r -range of 1.5–10 Å.

x	0	0.05	0.10	0.15
R_w (%)	13.4	17.0	17.2	17.8
a (Å)	3.2500(2)	3.25028(5)	3.2504(1)	3.2506(1)
c (Å)	5.2101(4)	5.2109(1)	5.2115(3)	5.2119(3)
$u(\text{Mg})$	-	0.380(4)	0.379(4)	0.380(3)
$u(\text{Zn})$	0.3819(4)	0.3817(1)	0.3815(3)	0.3813(3)

tions were accounted for with fixed occupancy parameters. Table I summarizes the results of the 1.5–10 Å range fitting, and Fig. 8 shows the refinement profiles for ZnO and $\text{Zn}_{0.85}\text{Mg}_{0.15}\text{O}$. Refinements over wider r -ranges tended to yield higher R_w factors but the fit results were similar to those given in Table I. It can be mentioned that the obtained R_w 's near 20% are common for PDF refinements, even for well-crystallized materials. The R_w 's from the PDF and Rietveld refinements cannot be directly compared, but they serve the same purpose of finding out the best structure solution from a number of competing models with similar numbers of refinable parameters.^{38,40} The inherently higher R_w in the PDF analysis stems from the greater sensitivity to the local atomic ordering, imperfect data correction, and systematic errors.³⁸ The R_w 's for the $\text{Zn}_{1-x}\text{Mg}_x\text{O}$ ($x > 0$) samples are significantly higher than that for ZnO ($x = 0$). It implies the presence of irregular Mg/Zn distribution in the alloy phases, which may not be well portrayed by simple structure models.

For all the four compositions, the lattice constants from the PDF agree well with the Rietveld refinement results, although the precision is slightly lower in PDF. Moreover the Zn atomic position and the Zn–O bond distances in ZnO are well reproduced in the PDF analysis, when compared with Rietveld refinement results. For the $\text{Zn}_{1-x}\text{Mg}_x\text{O}$ phases, the z -coordinates of Zn and Mg were independently refined to investigate the distinct local geometries of the two cation types. Interestingly the refined $u(\text{Mg})$ is smaller than $u(\text{Zn})$ for all the three solid solutions with $x = 0.05, 0.10,$ and 0.15 (Fig. 9). This trend is consistently repeated in the supercell model analyses detailed below. The $u(\text{Mg})$ parameters have rather large estimated deviations together with weak variations depending on x , but the observation $u(\text{Mg}) < u(\text{Zn})$ was quite robust regardless of the refinement r -range or the choice of constraints.

We recognize that in the above simple cell model for $\text{Zn}_{1-x}\text{Mg}_x\text{O}$, only the cation sub-lattices can be distorted while the anion framework remains undistorted. The wurtzite structure is its own antitype where the cation and anion sublattices are interchangeable. Depending on which of the two is distorted the resulting PDFs will be slightly different from each other, although the corresponding average crystal structures are practically indis-

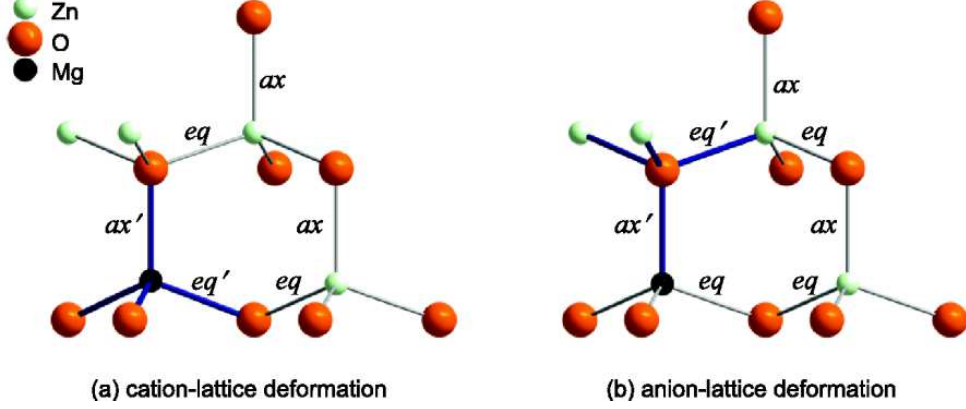


FIG. 10: (Color online) Local structural distortions in $\text{Zn}_{1-x}\text{Mg}_x\text{O}$ supercells of (a) cation-lattice deformation, $u(\text{Mg}) \neq u(\text{Zn})$, $u(\text{O}_{\text{Mg}}) = u(\text{O}_{\text{Zn}})$ and (b) anion-lattice deformation, $u(\text{Mg}) = u(\text{Zn})$, $u(\text{O}_{\text{Mg}}) \neq u(\text{O}_{\text{Zn}})$. ax and eq denote the cation–anion distances with different bond orientations, $\parallel c$ and $\perp c$, respectively. As resulted from local distortions, $ax' \neq ax$ and $eq' \neq eq$.

tinguishable. In case the oxygen-lattice is distorted, the partial PDF from O–O pairs is modified from that of the average crystal structure, and likewise, distortion of the cation-lattice affects the PDF for (Zn,Mg)–(Zn,Mg) pairs. The differentiations of cation–anion bond lengths in $\text{Zn}_{1-x}\text{Mg}_x\text{O}$, resulting from those two deformation cases, are illustrated in Fig. 10. In order to verify the lattice deformation type, we have examined the PDF refinements of $\text{Zn}_{0.85}\text{Mg}_{0.15}\text{O}$ using two different supercell models of $\text{Zn}_{15}\text{Mg}_3\text{O}_{18}$. In the anion-lattice deformation model, the z -coordinates of Zn and Mg atoms were fixed to 0 or $\frac{1}{2}$, but the z -coordinates of O atoms were refined with constraints; the three O atoms (O_{Mg}) that are apical to Mg were bound to have symmetry-related z -coordinates ($z_j = z_i$ or $z_i + \frac{1}{2}$), and so were the other fifteen O atoms (O_{Zn}). In the cation-lattice deformation model, the z -coordinates of O atoms were fixed, while the Zn and Mg positions were allowed to vary in independent groups. For each model, PDF refinements were carried out for the r -ranges from 1.5 Å to various r_{max} of 6.4–21.4 Å. Attempts using the smaller r_{max} (< 6 Å) suffered instability of the lattice constants, and were discarded. Since the resolution factor was very sensitive to the r_{max} , it was fixed to 0.1 in all the refinements.

The refinement results using the two supercell models are presented in Fig. 11. For both models, the R_w factors were obtained in the range of 17~19.5% with no apparent r_{max} -dependences. The two models are based on the deformation of different sublattices, and accordingly the z -coordinates of either cation or anion are presented for each. However, it can be well assumed that $u(\text{Mg})$ and $u(\text{Zn})$ from the cation-lattice deformation model are comparable respectively to $u(\text{O}_{\text{Mg}})$ and $u(\text{O}_{\text{Zn}})$ from the anion-lattice deformation. As shown in Fig. 11, the two supercell models similarly indicate that $u(\text{Mg}) < u(\text{Zn})$ and $u(\text{O}_{\text{Mg}}) < u(\text{O}_{\text{Zn}})$, namely that the axial Mg–O bonds are shorter than the axial Zn–O bonds. A quick examination of Fig. 11 reveals that the cation-

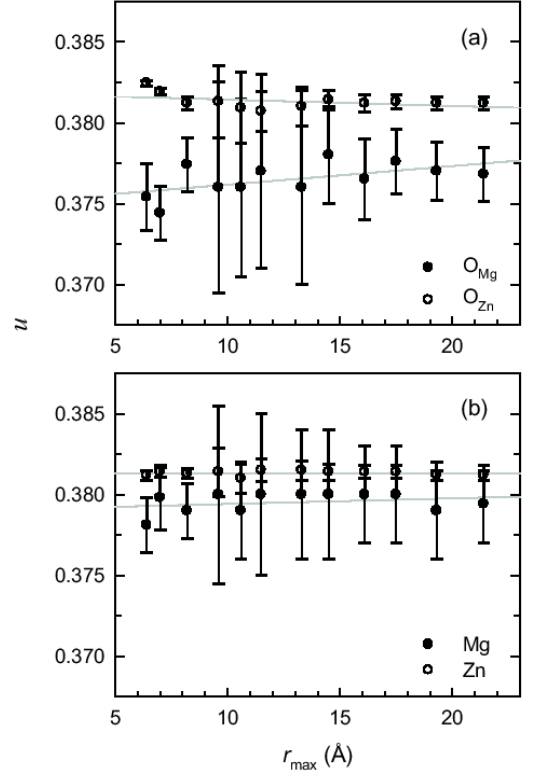


FIG. 11: Atomic positions in $\text{Zn}_{0.85}\text{Mg}_{0.15}\text{O}$ as functions of the length of the vector r_{max} . PDF refinements were carried out using the supercell model structures based on (a) anion-lattice deformation and (b) cation-lattice deformation. Gray lines are best linear fits.

lattice deformation model provides more reproducible refinements of atomic positions. The averages over the r_{max} -dependent refinement results are $u(\text{Mg}) = 0.3795(6)$ vs. $u(\text{O}_{\text{Mg}}) = 0.3765(10)$ and $u(\text{Zn}) = 0.3813(1)$ vs. $u(\text{O}_{\text{Zn}}) = 0.3813(5)$. The comparison of lattice constants

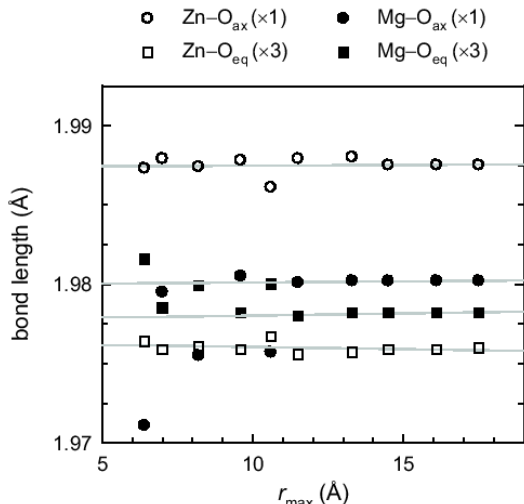


FIG. 12: Zn–O and Mg–O bond distances in $\text{Zn}_{0.85}\text{Mg}_{0.15}\text{O}$, obtained from the PDF refinements using the cation-lattice deformation supercell model. Gray lines are guides to the eye.

(not shown) further showed that the anion-lattice deformation model yields more scattered results. It is therefore judged that the cation-lattice deformation is appropriate for analyzing the $\text{Zn}_{1-x}\text{Mg}_x\text{O}$ structure.

Here it can be instructive to compare the local distortions in both deformation models in detail. In the cation-lattice deformation model (Fig. 10a), the bonding geometries of cations are differentiated simply by the atom type, Zn or Mg. On the other hand the anion-lattice deformation (Fig. 10b) creates three cation groups having different bonding geometries; (i) three Mg atoms, (ii) nine Zn atoms that are bonded to O_{Mg} , and (iii) six Zn atoms that are not bonded to O_{Mg} . For each cation group, the four nearest anion distances are slightly different, (i) $ax' + 3eq$, (ii) $ax + 2eq + eq'$, and (iii) $ax + 3eq$, using the notations in Fig. 10. However, the groups (i) and (iii) have same bond angles about the cation. It might be possible that the Zn atoms (ii and iii) have non-uniform coordination geometries depending on the proximity to the Mg, but it is hardly expected that Zn (iii) and Mg (i) have the same bond angles. In this regard, the coordination geometries of Zn and Mg are not sensibly distinguished in the anion-lattice deformation model. In Fig. 12, the Zn–O and Mg–O bond distances in $\text{Zn}_{0.85}\text{Mg}_{0.15}\text{O}$ are plotted as obtained from the cation-lattice deformation model. The refined structural parameters (a, c, u) were used to calculate the bond distances. For both Zn and Mg, the first coordination shells consist of one longer (c -axial) bond and three shorter (equatorial) bonds. As reflected by the difference between the longer and shorter bonds, Mg atoms are found to sit in more regular tetrahedra of oxygen than are Zn atoms.

IV. DISCUSSION

For various AX -type compounds including ZnO and MgO, the relative stabilities of wurtzite, zinc blende, and rock salt structures have been a long-standing and intriguing subject.^{41,42,43} The correlations between the binary composition and the favored structure type have been proposed in several different ways, but commonly using the bond ionicity and the ion sizes of A and X as the principal parameters.^{41,42,43} If we limit our attention to ZnO and MgO, the observed crystal structures can be explained simply by the ionicity consideration, in other words, electronegativities of Zn and Mg. With intermediate electronegativity, Zn can achieve the tetrahedrally directed valence orbital *via* facile sp^3 -hybridization. On the other hand, Mg is more electropositive and its valence orbital is dominated equally by the $3p_x$, $3p_y$, and $3p_z$ components, by which the nearest oxide ions are oriented in the octahedral geometry. Hence Zn and Mg adopt the four- and six-fold coordinations, respectively, in their binary oxides. Given those coordination preferences, the alloying with MgO should destabilize the host ZnO lattice. Indeed the thermodynamic solubility limit in $\text{Zn}_{1-x}\text{Mg}_x\text{O}$ is reached at a low Mg-concentration, $\approx 15\%$.^{2,44}

The ZnO has wurtzite parameters of $c/a = 1.6021$ and $u = 0.3829$, which are ideally 1.633 and 0.375, respectively.² Considering the range of c/a (1.600~1.645) observed from the binary wurtzites,⁴⁵ ZnO is near the borderline of wurtzite stability. On the other hand, the wurtzite MgO structure is not available experimentally. Instead, the first-principle methods based on density functional theory (DFT) have predicted that the wurtzite MgO will have much smaller c/a than those of existing wurtzite phases. An earlier DFT study has reported an extremely distorted hexagonal structure ($c/a = 1.20$, $u = 0.5$) for the wurtzite MgO, in which Mg sits on a mirror plane and has a bi-pyramidal coordination.⁴⁶ However recent studies, independently conducted by Janotti *et al.*⁴⁷ and Gopal and Spaldin,⁴⁸ have reported $c/a = 1.51$ and $u = 0.398$. More relevant to our experimental work, Malashevich and Vanderbilt performed the geometry optimization of $\text{Zn}_{1-x}\text{Mg}_x\text{O}$ supercells ($x = 0, \frac{1}{6}, \frac{1}{4}, \frac{1}{3},$ and $\frac{1}{2}$).⁴⁹ They showed that the c/a decreases with increase of Mg content, and $u(\text{Mg})$ is larger than $u(\text{Zn})$ in all the supercell compositions. Therefore those DFT studies on MgO and $\text{Zn}_{1-x}\text{Mg}_x\text{O}$ consistently surmise that the Mg-substitution in ZnO would result in the decrease of c/a , in agreement with the previously established idea that the c/a deviates farther from the ideal, when the bonding character becomes more ionic.⁵⁰ Our Rietveld study on $\text{Zn}_{1-x}\text{Mg}_x\text{O}$ has also shown that c/a is gradually decreased with the Mg-substitution.² The Mg-substitution in ZnO is not disfavored from packing considerations, but may reduce the electrostatic stabilizations in the long range through the change in c/a ratio. At the solubility limit $\text{Zn}_{0.85}\text{Mg}_{0.15}\text{O}$, the c/a is as low as 1.600, and this value seems to represent the lowest

c/a that can be sustained by the wurtzite lattice.

The energy-minimized $\text{Zn}_{1-x}\text{Mg}_x\text{O}$ supercells of Malashevich and Vanderbilt⁵¹ have $u(\text{Mg})$ in the range 0.387~0.390, and the $u(\text{Zn})$, 0.378~0.382, which is not in agreement with the PDF results shown in Figs. 9 and 11. As a consequence of $u(\text{Mg}) > u(\text{Zn})$, the spontaneous polarization in the computed $\text{Zn}_{1-x}\text{Mg}_x\text{O}$ supercells become larger for the compositions with higher Mg content,⁴⁹ while the Rietveld analysis indicated that the u parameter of $\text{Zn}_{1-x}\text{Mg}_x\text{O}$ average structures and therefore the spontaneous polarization in the Clausius-Mosotti limit decrease upon Mg-substitution.² The above discrepancies are in fact connected with a more fundamental question of how the tetrahedral geometries of ZnO_4 and MgO_4 would differ in the extended solids. Understanding of cation local geometries in $\text{Zn}_{1-x}\text{Mg}_x\text{O}$ is important also for the application of $\text{ZnO}/\text{Zn}_{1-x}\text{Mg}_x\text{O}$ heterojunction devices. While tetrahedral MgO_4 is found in a few minerals such as MgAl_2O_4 , $\text{Ca}_2\text{MgSi}_2\text{O}_7$,⁵² and $\text{K}_2\text{MgSi}_5\text{O}_{12}$,⁵³ $\text{Zn}_{1-x}\text{Mg}_x\text{O}$ provides an opportunity to explore its equilibrated tetrahedral geometry. However the computational and experimental results on the internal tetrahedral geometry of $\text{Zn}_{1-x}\text{Mg}_x\text{O}$ do not agree well. In the supercell structures of Malashevich and Vanderbilt,⁵¹ the ZnO_4 tetrahedra are more regular than the MgO_4 tetrahedra (as judged from the differences of the cation–anion bond distances), in contrast to the PDF findings presented in Fig. 12. These points may be further clarified by using alternative techniques such as neutron PDF or extended x-ray absorption fine structure. It is equally possible that the DFT methods must be re-examined, with inclusion of perhaps more accurate exchange functionals.

V. CONCLUSION

Raman and synchrotron x-ray PDF have been employed to probe the local structures of Zn and Mg atoms

that occupy the common crystallographic site in the wurtzite alloys $\text{Zn}_{1-x}\text{Mg}_x\text{O}$ ($x = 0, 0.05, 0.10,$ and 0.15). Regardless of the Mg concentration, structure model, and r -range, the PDF refinements consistently show that the Mg atoms have smaller out-of-center tetrahedral displacements than the Zn atoms. Even for the $\text{Zn}_{0.95}\text{Mg}_{0.05}\text{O}$ that has only 5 mol% MgO, the atomic coordinates of Zn and Mg were similarly obtained as those for $\text{Zn}_{0.90}\text{Mg}_{0.10}\text{O}$ and $\text{Zn}_{0.85}\text{Mg}_{0.15}\text{O}$, thereby demonstrating the fidelity of PDF technique. It is understood that the lessened tetrahedral distortion of MgO_4 , compared with ZnO_4 , leads to the decrease of wurtzite u parameters in the $\text{Zn}_{1-x}\text{Mg}_x\text{O}$ average structures. The hexagonal c/a ratio of $\text{Zn}_{1-x}\text{Mg}_x\text{O}$ decreases with the increase of Mg concentration, which is ascribed to the ionic character contributed from MgO. Therefore, from both ionicity and dipole strength viewpoints, we expect that the $\text{Zn}_{1-x}\text{Mg}_x\text{O}$ alloys will have smaller spontaneous polarizations than ZnO. It is noted that in terms of ZnO_4 and MgO_4 local geometries, our experimental results are somewhat contrary to the descriptions obtained from DFT-based studies.

Acknowledgments

The authors gratefully acknowledge discussions with Andrei Malashevich and David Vanderbilt and support from the National Science Foundation through the MRSEC program (DMR05-20415). K.P. has been supported by an NSF Graduate Student Fellowship. Work at Argonne National Laboratory and the Advanced Photon Source was supported by Department of Energy, Office of Basic Energy Sciences under Contract No. W-31-109-Eng.-38. The authors thank Peter Chupas and Karena Chapman for the help with synchrotron data collection.

-
- ¹ S. Rajan, H. Xing, S. DenBaars, U. K. Mishra, and D. Jena, *Appl. Phys. Lett.* **84**, 1591 (2004).
- ² Y.-I. Kim, K. Page, and R. Seshadri, *Appl. Phys. Lett.* **90**, 101904 (2007).
- ³ S. Rohmfeld, M. Hundhausen, and L. Ley, *Phys. Rev. B* **58**, 9858 (1998).
- ⁴ M. Franz, K. F. Dombrowski, H. Rucker, B. Dietrich, K. Pressel, A. Barz, U. Kerat, P. Dold, and K. W. Benz, *Phys. Rev. B* **59**, 10614 (1999).
- ⁵ H. Richter, Z. P. Wang, and L. Ley, *Solid State Commun.* **39**, 615 (1981).
- ⁶ K. K. Tiong, P. M. Amirtharaj, F. H. Pollak, and D. E. Aspnes, *Appl. Phys. Lett.* **44**, 122 (1983).
- ⁷ T. R. Yang, C. C. Lu, W. C. Chou, Z. C. Feng, and S. J. Chua, *Phys. Rev. B* **60**, 16058 (1999).
- ⁸ C. Ramkumar, K. P. Jain, and S. C. Abbi, *Phys. Rev. B* **53**, 13672 (1996).
- ⁹ S. J. L. Billinge and M. G. Kanatzidis, *Chem. Commun.* 749 (2004).
- ¹⁰ X. Qiu, E. S. Bozin, P. Juhas, Th. Proffen, S. J. L. Billinge, *J. Appl. Crystallogr.* **37**, 110 (2004).
- ¹¹ D. A. Shirley, *Phys. Rev. B* **5**, 4709 (1972).
- ¹² V. Lughii and D. R. Clarke, *J. Am. Ceram. Soc.* **88**, 2552 (2005).
- ¹³ A. P. Hammersley, S. O. Svensson, M. Hanfland, A. N. Fitch, and D. Hausermann, *High Press. Res.* **14**, 235 (1996).
- ¹⁴ X. Qiu, J. W. Thompson, S. J. L. Billinge, *J. Appl. Crystallogr.* **37**, 678 (2004).
- ¹⁵ Th. Proffen and S. J. L. Billinge, *J. Appl. Cryst.* **32**, 572 (1999).
- ¹⁶ D. Dollimore and D. Nicholson, *J. Chem. Soc.* 960 (1962).
- ¹⁷ A. L. Smith, in *The Coblenz Society Desk Book of Infrared Spectra*, 2nd ed., edited by C. D. Carver (The

- Coblenz Society, Kirkwood, MO, 1982), pp. 1–24. See also <http://webbook.nist.gov/>
- ¹⁸ W. M. Hlaing Oo, M. D. McCluskey, A. D. Lalonde, and M. G. Norton, *Appl. Phys. Lett.* **86**, 073111 (2005).
 - ¹⁹ J. Saussey, J.-C. Lavalley, and C. Bovet, *J. Chem. Soc., Faraday Trans.* **78**, 1457 (1982).
 - ²⁰ P. Kubelka and F. Munk, *Z. Tech. Phys.* **12**, 593 (1931).
 - ²¹ A. Ohtomo, M. Kawasaki, T. Koida, K. Masubuchi, H. Koinuma, Y. Sakurai, Y. Yoshida, T. Yasuda, and Y. Segawa, *Appl. Phys. Lett.* **72**, 2466 (1998).
 - ²² V. Srikant and D. R. Clarke, *J. Appl. Phys.* **83**, 5447 (1998).
 - ²³ D. J. Singh, R. C. Rai, J. L. Musfeldt, S. Auluck, N. Singh, P. Khalifah, S. McClure, and D. G. Mandrus, *Chem. Mater.* **18**, 2696 (2006).
 - ²⁴ J. M. Calleja and M. Cardona, *Phys. Rev. B* **16**, 3753 (1977).
 - ²⁵ T. C. Damen, S. P. S. Porto, and B. Tell, *Phys. Rev.* **142**, 570 (1966).
 - ²⁶ J. M. Zhang, T. Ruf, M. Cardona, O. Ambacher, M. Stutzmann, J.-M. Wagner, and F. Bechstedt, *Phys. Rev. B* **56**, 14399 (1997).
 - ²⁷ K. Ishikawa, N. Fujima, and H. Komura, *J. Appl. Phys.* **57**, 973 (1985).
 - ²⁸ C. Bundesmann, N. Ashkenov, M. Schubert, D. Spemann, T. Butz, E. M. Kaidashev, M. Lorenz, and M. Grundmann, *Appl. Phys. Lett.* **83**, 1974 (2003).
 - ²⁹ A. Kaschner, U. Haboexk, M. Strassburg, G. Kaczmarczyk, A. Hoffmann, C. Thomsen, A. Zeuner, H. R. Alves, D. M. Hofmann, and B. K. Meyer, *Appl. Phys. Lett.* **80**, 1909 (2002).
 - ³⁰ C.-J. Pan, H.-C. Hsu, H.-M. Cheng, C.-Y. Wu, and W.-F. Hsieh, *J. Solid State Chem.* **180**, 1188 (2007).
 - ³¹ M. S. Tomar, R. Melgarejo, P. S. Dobal, and R. S. Katiyar, *J. Mater. Res.* **16**, 903 (2001).
 - ³² L. Bergman, M. D. Bremser, W. G. Perry, R. F. Davis, M. Dutta, and R. J. Nemanich, *Appl. Phys. Lett.* **71**, 2157 (1997).
 - ³³ J. Serrano, F. J. Manjon, A. H. Romero, F. Widulle, R. Lauck, and M. Cardona, *Phys. Rev. Lett.* **90**, 055510 (2003).
 - ³⁴ Th. Gruber, G. M. Prinz, C. Kirchner, R. Kling, F. Reuss, W. Limmer, and A. Waag, *J. Appl. Phys.* **96**, 289 (2004).
 - ³⁵ K. Samanta, P. Bhattacharya, R. S. Katiyar, W. Iwamoto, P. G. Pagliuso, and C. Rettori, *Phys. Rev. B* **73**, 245213 (2006).
 - ³⁶ T. R. Welberry and B. D. Butler, *Chem. Rev.* **95**, 2369 (1995).
 - ³⁷ F. Frey, *Acta Crystallogr., Sect. B: Struct. Sci.* **51**, 592 (1995).
 - ³⁸ T. Egami and S. J. L. Billinge, *Underneath the Bragg Peaks: Structural Analysis of Complex Materials*. (Pergamon, Amsterdam, 2003).
 - ³⁹ P. J. Chupas, X. Y. Qiu, J. C. Hanson, P. L. Lee, C. P. Grey, and S. J. L. Billinge, *J. Appl. Crystallogr.* **36**, 1342 (2003).
 - ⁴⁰ V. Petkov, M. Gateshki, M. Niederberger, and Y. Ren, *Chem. Mater.* **18**, 814 (2006).
 - ⁴¹ J. C. Phillips, *Rev. Mod. Phys.* **42**, 317 (1970).
 - ⁴² E. Mooser and W. B. Pearson, *Acta Crystallogr.* **12**, 1015 (1959).
 - ⁴³ M. O’Keeffe and B. G. Hyde, *Acta Crystallogr., Sect. B: Struct. Sci.* **34**, 3519 (1978).
 - ⁴⁴ Yu. P. Sapozhnikov, Yu. D. Kondrashev, L. Ya. Markovskii, and Yu. A. Omel’chenko, *Russ. J. Inorg. Chem.* **6**, 1289 (1961).
 - ⁴⁵ P. Lawaetz, *Phys. Rev. B* **5**, 4039 (1972).
 - ⁴⁶ S. Limpijumnong and W. R. L. Lambrecht, *Phys. Rev. B* **63**, 104103 (2001).
 - ⁴⁷ A. Janotti, D. Segev, and C. G. Van de Walle, *Phys. Rev. B* **74**, 045202 (2006).
 - ⁴⁸ P. Gopal and N. A. Spaldin, *J. Electron. Mater.* **35**, 538 (2006).
 - ⁴⁹ A. Malashevich and D. Vanderbilt, *Phys. Rev. B* **75**, 045106 (2007).
 - ⁵⁰ H. Schulz and K. H. Thiemann, *Solid State Commun.* **23**, 815 (1977).
 - ⁵¹ A. Malashevich and D. Vanderbilt, private communications.
 - ⁵² M. Kimata and N. Ii, *Neues Jahrb. Miner. Monatsh.* **1** (1981).
 - ⁵³ A. M. T. Bell, C. M. B. Henderson, S. A. T. Redfern, R. J. Cernik, P. E. Champness, A. N. Fitch, and S. C. Kohn, *Acta Crystallogr., Sect. B: Struct. Sci.* **50**, 31 (1994).